Low-cost, Electro-Active C@Fe_3C/Fe_3O_4 composite derived using bagasse for the oxygen reduction reaction

Sai Rashmi Manippady,[a] Ziyauddin Khan,[b] Akshaya Kumar Samal,[a] Manav Saxena*[a]

[a] Centre for Nano and Material Sciences, Jain University, Bengaluru, Karnataka-562112, India.

[b] Laboratory of Organic Electronics, Department of Science and Technology, Linköping University, Norrköping, SE-60174 Sweden

Corresponding author email:

manavsaxena19@gmail.com; s.manav@jainuniversity.ac.in (MS)

Abstract

As the world is heading towards a sustainable future, it is highly important to develop low-cost electrocatalysts for energy generation devices. Herein, we report the synthesis of iron-carbon hybrid (C@Fe_3C/Fe_3O_4) nanocomposite for oxygen reduction reaction (ORR), synthesized using bagasse as a carbon source material and Fe(III) precursor at 900 ˚C. The synthesized C@Fe_3C/Fe_3O_4 composite exhibits a high surface area of ~930 m^2/g. The electrode material has a 0.86 V overpotential vs RHE. Moreover, the electrocatalyst shows catalytic stability upto 18 h at the static potential of 0.25 V vs RHE at the rotation speed of 1600 rpm. Herein, the electron transfer number is close to 4 which suggests that our electrocatalyst may have an impact on efficient electrocatalyst designing for ORR in alkaline solution.

1. Introduction

The world's energy need is fuelled by fossil fuels, yet consumption is skyrocketing owing to population growth. There has been growing upsurge towards upgradation of the renewable energy technologies in order to counter the future energy crisis caused due to exponentially increased populations. In this regards, regenerative fuel cells[1, 2] and rechargeable metal-air batteries[3, 4] are the most promising energy storage and conversion pathways that has potential to fulfil required energy demands. Moreover, the oxygen reduction reactions (ORR) plays an important role towards the energy efficiency of the fuel cells.[5] However, kinetics and feasibility of electrochemical reactions during energy conversion in these devices has great impact to their performances. ORR is an important half-cell reaction in energy devices but on contrary have sluggish reaction kinetics due to strong O=O bond. Acceleration of this reaction becomes a question of optimizing reaction rates using different metals as electrocatalyst for driving the reaction in the forward direction. To accelerate the kinetics, different metals must be used to optimise reaction rates, as the reaction requires an additional electrocatalyst to drive it forward. Platinum (Pt), Palladium (Pd) and Iridium (Ir)-based materials were extensively explored as electrocatalysts due to its excellent catalytic performances since they were thought to be the most effective electrocatalysts for ORR. The platinum percentage of commercial Pt/C catalysts ranged from 10 to 60% by weight, with a Pt loading of 0.4 to 0.8 mg Pt/cm^2. However, the expensive cost of Pt and the limited durability of support materials impede commercialization. Xiao et al. reported Pd based nanocatalyst with active sites which improves ORR performance by tuning strain and particle size.[6] However, Pd is very precious and is practically essential in catalytic converters in automobiles.[7] Beermann et al. reported good stability of shape-controlled Pt-Ni nanoparticles for ORR activity.[8] Although the catalyst meets good stability, it does not meet an approach to sustainability or practical feasibility due to its high cost. Zhang et al. reported single-atomic Ruthenium catalytic sites on nitrogen-doped graphene for ORR activity. The catalyst showed onset potential of 0.89V vs RHE with remarkable durability.[9] One possibility is to use transition metal-based and/or heteroatom-doped catalyst materials.

In the last decades, there have been several reports on non-precious electrocatalysts such as inorganic nanoparticles,[10-12] transition metal-nitrogen-carbon catalysts,[13-15] transition metal oxides,[16, 17] non-metal (N, P, S, F etc) doped carbon materials,[18-21] CNT,[22, 23] metal organic framework (MOF) based porous carbon[24-27] etc based electroactive materials have gained significant attention in order to overcome the cost and sluggish reaction kinetics of ORR. The carbon-based catalysts have attracted a greater attention because of its decent catalytic activity, low capital consumption and longer durability.[28]

Among several catalysts, non-precious metal catalysts (NMPCs) are ideal for ORR as it satisfies the following crucial requirements: (i) enough active sites to enhance ORR kinetics and comparable results noble-metal catalysts; (ii) close to 4 e^- reduction pathway ; (iii) long term stability and superior tolerance to methanol/CO poisoning compared to that of noble metal catalysts[29]. In particular, carbon-based catalysts with heteroatoms/transition metals (e.g. Fe and/or Co) [30-32] are the best alternatives as ORR catalysts. Nevertheless, further improvement in view of synthetic feasibly, material cost and catalytic performances remains an exciting and interesting cause for developing new electro-active materials towards ORR.

Biomass-derived carbon is one of the previously stated support materials that has recently attracted a lot of attention. [33-36] Lignin-rich biomass has been shown to be an excellent precursor for high surface area carbon synthesis. The majority of agriculture-industry by-products are traditionally burnt, so there is a compelling need to explore more efficient ways to commodify numerous by-products. This could also aid in the replacement of precious catalyst carriers in energy conversion systems with greener and less expensive biomass-based materials with strong electrocatalytic activity.

To overcome all the challenges, herein, we report a simple and sustainable carbon-transition metal oxide composite material using a waste agricultural, biomass material "bagasse *(Saccharum officinarum)*" via carbonization process in N_2 atmosphere without any KOH activation step. Bagasse is dry fibrous residue made up of 32-34% cellulose, 19-24% hemicellulose, 25-32% lignin, 6-12% extractives, and 2-6% ash that remains after sugarcane stalks are crushed to extract juice.[37, 38] The oxygen moieties present in the bagasse coordinates with Fe^{3+} ions and helps in homogenous distribution of iron oxides during the carbonization. Interestingly, composite material showed an impressive overpotential of 0.86 V vs RHE in 0.1 M KOH. The composite shows the catalytic stability upto 18 h at the static potential of 0.25 V vs RHE at rotation speed of 1600 rpm. The electron transfer number is close to 4 which suggest that synthesized electrocatalyst might be prominent application. The present work provides useful insight to design carbon based electrocatalyst.

2. Experimental section

2.1 Synthesis of the composite material

5g of powdered bagasse was soaked in 20 mL $Fe(NO_3)_3.9H_2O$ solution with known concentration of Fe^{3+} for 24 h. Three samples were prepared by choosing 5%, 10 and 30% (wt%) of Fe-precursor (w.r.t. bagasse weight). The iron treated bagasse were dried in hot air oven at 60 ˚C for 12h followed by carbonization at 900 ˚C (heating rate of 10 ˚C/min) in a quartz tube furnace under a continuous flow of N_2 at 1 atm pressure. After maintaining furnace at 900 °C for an hour, the furnace was allowed to cool to RT under continuous N_2 flow. The 'control' sample was also synthesized without Fe-precursor. The iron-treated samples were referred to **CF1**, **CF2** and **CF3**, which represents the 5, 10 and 30% (wt% wrt bagasse weight) of iron precursor respectively. The mass percentages of iron in 5, 10 and 30% (wt%) samples with respect to total mass (iron salt + bagasse) are is 0.66, 1.26, and 3.2%.

2.2 Material Characterization

The Brunauer-Emmett-Teller (BET) surface area analyzer was used to record nitrogen sorption isotherms at 77 K. (Bellsorp Max, Japan). Pore size distribution plots were taken from the desorption isotherms using the Barrett-Joyner-Halenda (BJH) model. The samples were degassed for 12 hours at 200 °C under vacuum before to measurement. Powder X-ray diffraction (PXRD) with Cu-K_α radiation was recorded across a range of 5-80º with a scan speed of 3°/min (Rigaku X-ray diffraction ultima-IV, Japan). Thermo ScientificTM TalosTM F200S High-Resolution Transmission Electron Microscope was used to examine the surface morphology of the samples (HRTEM). The PHI 5000 Versa ProbII, FEI Inc., was used to perform X-ray photoelectron spectroscopic (XPS) characterization. Raman spectra was recorded using Horiba Jobin Yvon Xplora Plus V1.2 Multiline with 532 nm excitation wavelength. Electrochemical characterization was performed using OrigaLys ElectroChem multichannel workstation equipped with Autolab RRDE setup.

2.3 Electrochemically catalyzed ORR:

The ORR experiment was performed in a three-electrode system using an aqueous solution of 0.1 M KOH. Glassy carbon (GC) electrode was used as working electrode. Whereas, platinum (Pt) and Hg/HgO electrode were served as counter and reference electrode, respectively. Electrocatalytic ink was prepared by mixing of 1 mg active material with 1 mg volcan carbon in the solvent mixture of water (200 µl) and isopropanol (200µl). Next, 6 µl of Nafion was added which acts as a binder. The mixture was sonicated for 30 minutes in order to get fine dispersion before using for electrocatalytic studies. Now, 4 µl of freshly prepared electrocatalytic ink was drop casted over the GC electrode (working electrode) and allowed to dry for 3h at ambient condition. This GC electrode coated with electrocatalyst was used for electrochemical studies. All the electrochemical experiments were performed at the scan rate of 5 mV/s. Cyclic voltammetry (CV) experiments were done at static conditions whereas, linear sweep voltammetry (LSV) was performed at different rotation speeds in continuous flow of O_2. All the electrochemical data were plotted with respect to the reversible hydrogen electrode (RHE).

Oxygen Reduction Reaction:

The reference electrode was calibrated with respect to the reversible hydrogen electrode (RHE). All potentials were rescaled to the pH-independent reversible hydrogen electrode (RHE). The long-term stability for ORR catalysis was evaluated by chronoamperometry, performed in 0.1 M KOH solution at a static potential of 0.25V. To avoid accumulation of gas bubbles on the electrode surface, the electrode was maintained at a rotation of 1600 rpm during the experiment. The number of electrons were calculated using K-L plot (see SI). Rotating ring disk electrode (RRDE) voltammetry was used to calculate the number of electrons and the amount of H_2O_2 formed during ORR based on the ratio of the disk and the ring current (see SI).

3. Results and discussion

Designing catalyst is one of the greatest challenge in any chemical reaction with understanding of different factors. We had designed the composite by using the coordinating ability of oxygen groups (methoxy, carboxyl, phenolic) from sugar and lignin moieties present in bagasse (a typical bio waste from the sugar industry) with Fe^{3+} ions, to synthesize active material. The Fe^{3+} ions interacted with oxygen groups and present homogeneously in the bagasse. During the carbonization process, iron oxide particles are evenly dispersed throughout the carbon precursor. The synthesis process, Fe^{3+} binding with bagasse and electrocatalytic application toward ORR is schematically represented in Figure 1 and further discussed.

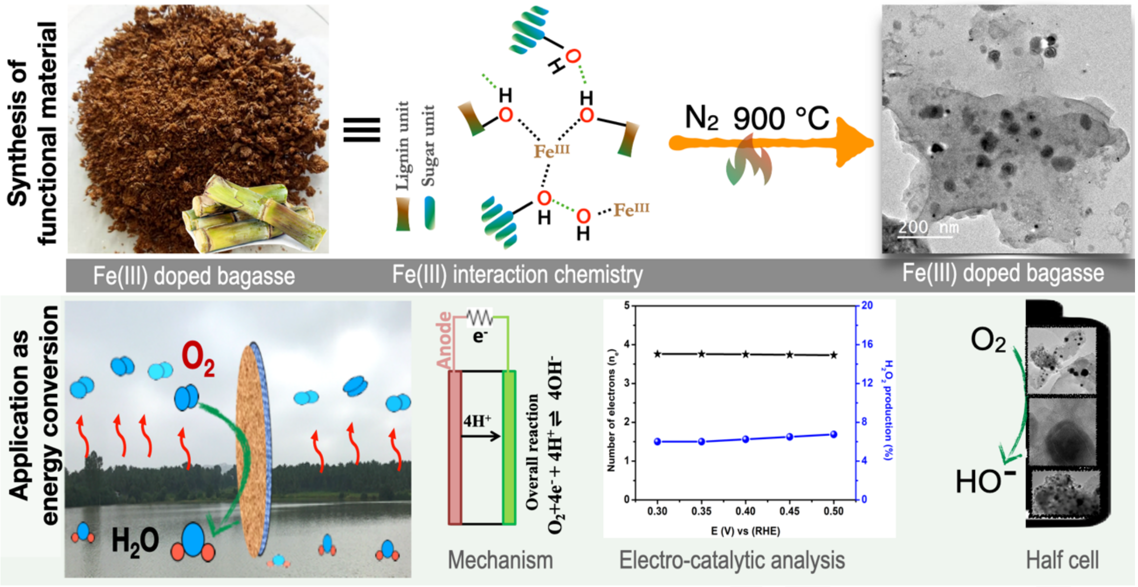

Figure1: Schematic representation for the synthesis of the functional composite material and ORR application.

The surface area and the pore size distribution of CF2 was characterize using N_2 adsorption-desorption at 77 K. The adsorption-desorption curves of CF-2 were ascribed to typical type II profile (Figure 2a). The surface area of CF2 is ~930 m^2g^{-1} which is ~25% higher compared to that of CF0 (~740 m^2g^{-1}). The maximal absorption of N_2 gas (77 K) by CF2 was determined to be 344 cc/g at 1 atm pressure. The pore size distribution (PSD) for CF2 revealed pore diameters in the range of 0.4-1.7 nm (Figure 2b), indicating micropore nature for the material. Table 1 lists the detailed textural characteristics of control, CF1, CF2, and CF3. The presence of nanoparticles on the carbon surface may plug the pores, resulting in decreased in surface area as the iron content increases.

Table 1: Textural properties of Control, CF1, CF2 and CF3.

Textural properties	Control	CF1	CF2	CF3
Surface area (m^2 g^{-1})	740	623	930	462
Total pore volume (cm^3 g^{-1})	0.330	0.319	0.533	0.505
Micropore size (nm)	1.2-1.8	1.0-1.5	0.4-1.7	1.0-1.5

PXRD analysis was performed to know the crystallinity and crystallographic structure of the control and CF2. Sharp peaks in CF2 suggest the crystalline nature of the material (Figure 2c). For CF-2, the sharp peaks at 2θ= 25.6˚, 44.6˚ and 57.2˚ corresponds to the (002), (101) and (004) planes of graphite.[39] The lattice spacing corresponds to (002) plane is 3.5 Å which is very close to the lattice spacing observed by HRTEM (3.7 Å). The peaks at 2θ= 37.6˚ and 43.1˚ corresponds to the (112) and (121) plane of Fe_3C (ref. code 01-085-0871). The peaks at 2θ= 30.2˚, 35.6˚, 45.7˚, 53.6˚, 62.7˚ corresponds to the (022), (131), (242) and (044) crystal planes of Fe_3O_4 (ref. code 96-900-5839). On the basis of PXRD analysis, the structural composition of CF2 could be written as $C@Fe_3C/Fe_3O_4$ composite. The presence of graphitic structure, Fe_3O_4 and Fe_3C as a hybrid structure is also supported through HRTEM analysis which is discussed later here. PXRD of control shows broad peaks at 2θ = 23.2˚ and 43.6˚ refers to the (002) and (100) planes suggesting the amorphous nature of control (Figure S1a). The process of Fe_3C synthesis and graphitization in CF2 is fascinating. Bagasse treated with Fe^{3+} ions includes a considerable number of O atoms, which lead to the nucleation/formation of iron oxide particles when heated to a higher temperature. These iron oxide particles now act as a nucleation site and stimulate the development of a graphitized layer outward. Carbon has temperature dependent solubility in iron. Carbon diffusion into iron oxide particles occurred simultaneously with the synthesis of iron oxides at higher temperatures. Upon cooling, carbon gets precipitated out as disordered graphitized structure and iron carbide. The schematic presentation of mechanism is shown in Figure 2d. Thus it follows ‘solution-dissolution’ mechanism.

Comparative Raman spectra of control and CF2 are shown in Figure 2e. The G band for control and CF2 are positioned at 1605 and 1593 cm^{-1} respectively. The D band of control and CF2 are positioned at 1350 and 1343 cm^{-1}. The FWHM of D-band of CF2 is 114 cm^{-1} as compared to 173 cm^{-1} of control. The formation of ordered structure causes the decrease in FWHM of the D-band, indicating the presence of graphitized structure. The presence of graphitized carbon structure, which is missing in control, is confirmed by a new peak at 2685 cm-1 matching to the 2D band that appears in CF2. PXRD and HRTEM analysis show that CF2 graphitization is likewise consistent.

In order to understand the chemical composition of CF2 material, X-ray photoelectron spectroscopy (XPS) was performed. The high-resolution Fe 2p spectrum of CF2 shows two broad peaks at 710.6 and 725.5 eV which are separated by split spin-orbit components of 14.9 eV (Figure 2f). The peak at 710.6 eV corresponds to Fe $2p_{3/2}$ which is in accordance with the previous report. [40] The broad nature of peak at 710.6 eV might be due to the combine $2p_{3/2}$ peak of Fe_3O_4 and Fe_3C (708.3 eV) [41]. The nature and peak position of high resolution O1s spectrum shows the peak maxima at 529 eV (Figure 2g) which is well matched with the literature report of Fe_3O_4. [40] The iron-content in CF2 is 1.82 at% as quantified by XPS which is in well agreement with the EDS analysis. The quantification of C, N, O and Fe has been tabulated in Table S1.

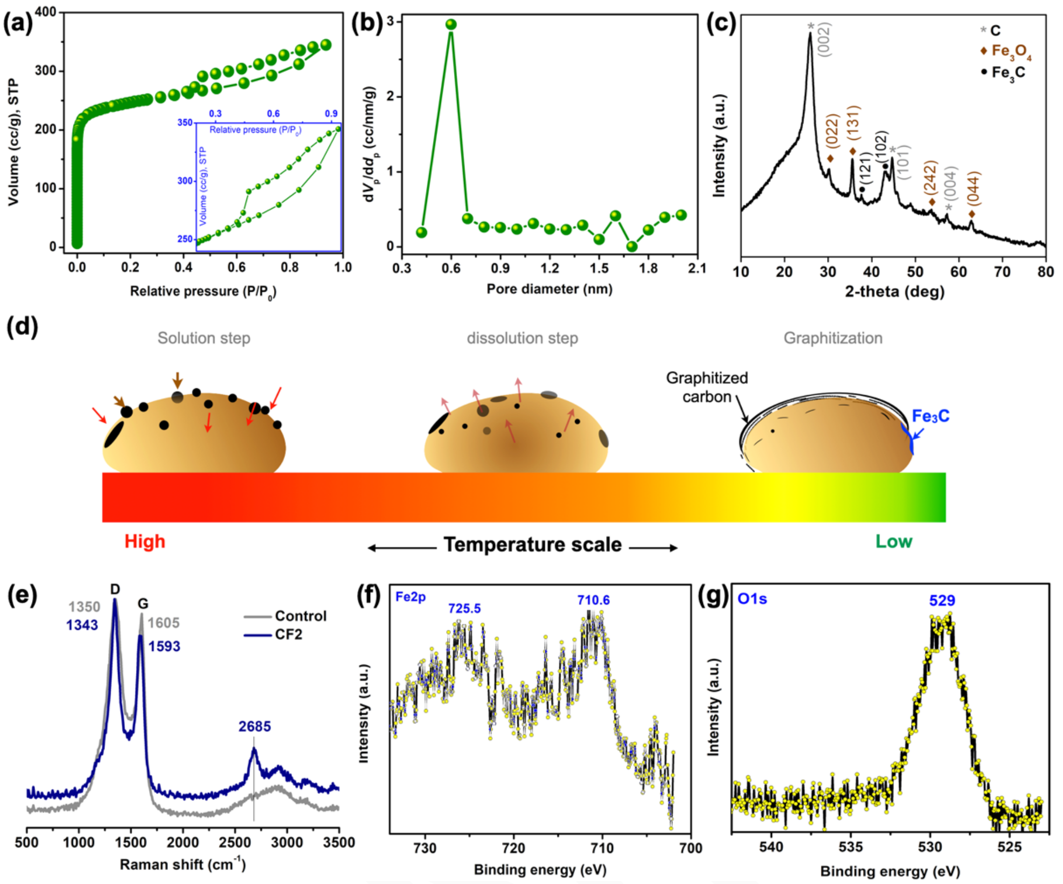

Figure 2: (a) N_2 adsorption-desorption (inset: magnified N_2 adsorption-desorption), (b) Pore size distribution, (c) PXRD of CF2, (d) Graphitization mechanism, (e) Raman spectra, XPS spectra (f) Fe 2p, (g) O 1s of CF2.

FESEM and HRTEM analysis were carried out to study the surface morphology of the composite. FESEM of control show irregular morphology whereas CF1, CF2 and CF3 confirms the presence of Fe_3O_4/Fe_3C particles embedded in the carbon structure. (Figure 3a-d). HRTEM analysis of control reveals the porous layered carbon structure (Figure 3e) which is amorphous in nature as suggested by diffuse ring SAED pattern of control material (Figure S1b). The amorphous nature and absence of graphitized carbon in control is supported by broad PXRD peaks (Figure S1a). Low and high magnification HRTEM of CF2 is shown in Figure 3 g,h. Figure 3g suggests that Fe_3O_4 nanoparticles (high contrast) are embedded homogeneously in the thin layer carbon matrix. The dense contrast area in Figure 3g is Fe_3O_4, whereas yellow arrows indicate the graphitized carbon layers in the CF2. The yellow and red coloured dotted area in Figure 3g is magnified and shown as Figure 3h and 3i respectively. The two different type of lattice-spacing 2.39 Å and 3.7 Å could be seen at the middle and edges of CF2 (Figure 3h). The lattice spacing of 2.39 Å corresponds to the (121) plane of Fe_3C (ref code 96-901-6232). The graphitic layers could be easily seen at the top-right corner adjacent to Fe_3C (Figure 3h). The 3.7 Å lattice spacing of graphitic layers corresponds to the (002) plane which is further corroborated with PXRD (Figure 2c). The lattice spacing is slightly higher than standard interlayer graphite distance (3.4 Å) suggests that graphitic layers in CF2 are defected. The presence of Fe_3C and graphitic layer together confirms the "solution-dissolution" based growth mechanism as discussed and represented in Figure 2d. The blue color marked area of Figure 3i is shown as Figure 3j where lattice fringes could be clearly visible suggested high crystallinity of the particle. The lattice spacing of 2.9 Å corresponds to the (022) plane of Fe_3O_4 (ref. code 96-900-5839). The graphitization of CF2 as per discussed 'solution-dissolution' mechanism is also confirmed by presence of the graphitized layers in the other regions as show in Figure 3k. The SAED pattern of CF2 exhibits characteristic diffraction spots for different planes of Fe_3O_4, Fe_3C, and graphitized carbon, confirming that the CF2 structure may be represented as $C@Fe_3C/Fe_3O_4$ composite. (Figure 3l). Energy-dispersive X-ray spectroscopy (EDS) analysis was also performed to quantify the C, N, O and Fe content in control and CF2. (Table S1). The iron content in control and CF2 are 0% and 1.3% (at.%) which is in well agreement with XPS data.

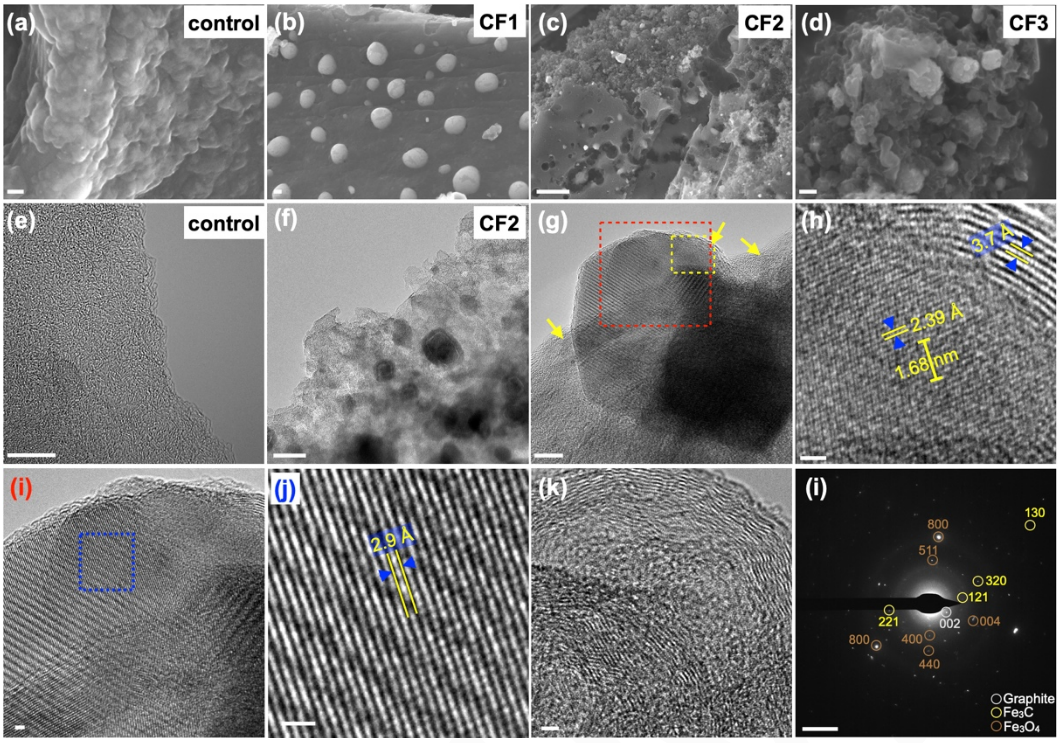

Figure 3: FESEM image of (a) control (b) CF1 (c) CF2 (d) CF3. HRTEM images of (e) control (f-k) CF2. (l) SAED pattern of CF2. Scale bar: (a-d) 100 nm, (e) 10 nm (f) 50 nm (g) 10 nm (h) 1 nm (i-k) 1 nm (l) 5 1/nm.

Electrochemical studies:

The electrochemical activity of synthesized carbons (control, CF1, CF2 and CF3) is first evaluated by cyclic voltammetry in O_2 saturated solution (Figure S3). All the samples show reduction peak at 0.61 V suggesting that the all the synthesized materials are electrochemically active. The current density increases with increase in the iron loading. The CV of CF2 recorded in the oxygen saturated electrolyte shows an intense reduction peak at 0.61 V vs RHE (Figure 4a). Notably, this peak is absent in the nitrogen saturated solution which unambiguously showed the potential of CF2 towards catalyzing the oxygen reduction reaction. To confirm the activity of synthesized active materials toward ORR, we had performed LSV of all the synthesized material at 1600 rpm. Among all the samples, CF2 shows highest current density of -7.7 mA/cm^2 as compared with the control (-3.2 mA/cm^2), CF1 (-5.5 mA/cm^2) and CF3 (-

4.5 mA/cm^2) (Figure 4b). The highest current density of CF2 suggests its superior electrocatalytic performance towards ORR and thus CF2 sample is used for further detailed electrochemical analysis. Further, LSV of CF2 was performed at different rotation speed. The LSV shows that limiting current increases with increasing rotation rate (Figure 4c). The LSV data of control, CF1, CF2 and CF3 is tubulised in Table 2. The current density at the highest rotation speed of 3600 rpm was found to be -9.1 mA/cm^2. The high current density values might be due to the abundant O_2 dissolution and diffusion in the electrolyte by continuous flow of O_2. [42] Importantly, the onset potential to initiate the ORR for CF2 was found to 0.86V vs RHE which is comparable to the recent literature reports (Table 3). reference At the same time, overpotential for catalyzing ORR would be 140 mV for the CF2. Notably, overpotential required for ORR and obtained current density for CF2 is comparable and in fact better than some of the reported electrocatalyst materials. Add some more [43, 44] Further, Koutecky-Levich (K-L) plot was derived from LSV plot in order to understand the kinetics of the ORR process. Notably, linearity of Koutecky-Levich (K-L) plot between j^{-1} and $\omega^{-1/2}$ is indicative for the first order reaction kinetics (Figure 4d). Further, the electron transfer number was also calculated by K-L plot which was found to be 3.73-3.76 in the potential range of 0.3-0.5 V vs RHE (Figure 4d). Typically, the benchmark electrocatalyst for ORR such as Pt/C utilized direct 4e- pathway [$O_2 + 2H_2O + 4e^- \leftrightarrow 4OH^-(aq)$] which does not proceed via formation of a peroxide intermediate. [45] Herein, the electron transfer number is close to 4 which suggest that our electrocatalyst can be a potential alternate to expensive Pt/C. This has further validated by the rotating ring and disc electrode (RRDE) experiment (Figure 4e). The number of electrons calculated between the potential range 0.3-0.5 V through RRDE experiment was found to be 3.73-3.76 (Figure 4f). Both, K-L plot and RRDE plot has clearly indicated that the ORR process catalyzed by CF2 is a four-electron process and therefore, water is expected to be the end product in the ORR process. Further, H_2O_2 formed during ORR was found to be 6-7% in the potential range 0.3-0.5 V (Figure 4f). Further, the catalytic stability test was performed for 18 h at the static potential of 0.25 V vs RHE at the rotation speed of 1600 rpm (Figure S4). After stabilizing the current in initial hours, the catalytic performance was found to be stable for 18 hrs which demonstrates excellent catalytic stability towards ORR process. The presence of graphitized carbon in CF2 is noteworthy that is expected to enhance the stability of the ORR catalysts. [46]

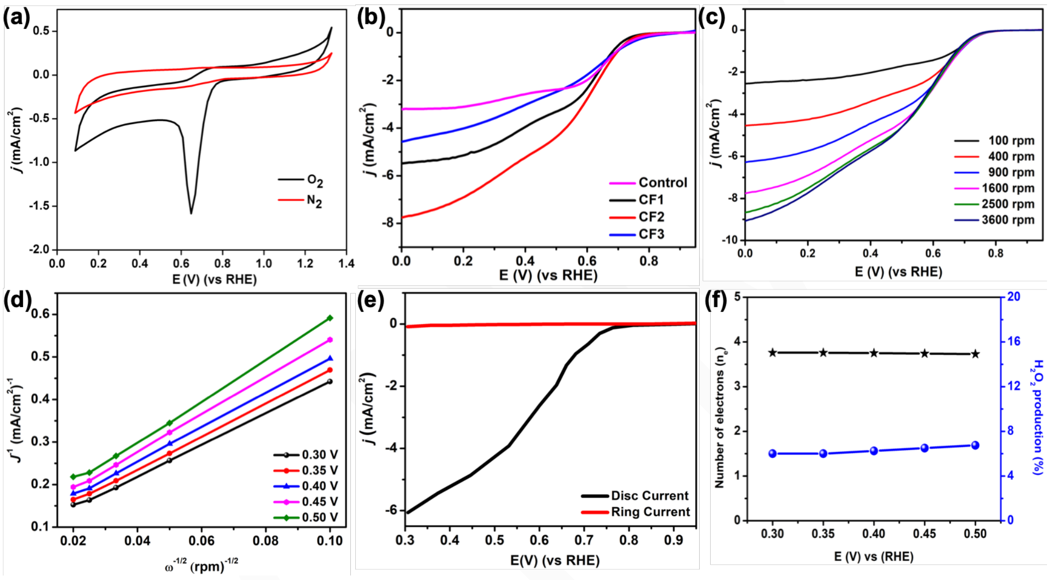

Figure 4: (a) CV of CF2 in N_2 and O_2-saturated solution; scan rate: 5 mV/s, (b) LSV of different samples at 1600 rpm. Electrochemical studies of CF2 (c) LSV at different scan speed, (d) K-L plots, (e) RRDE measurement in O_2-saturated solution (rotation speed: 1600 rpm), (f) Plot showing the average % of H_2O_2 production and number of electron transferred. All studies were performed at 0.1 M KOH solution.

Table 2: Current density of different active material @1600 rpm.

Comparative analysis of active material @1600 rpm				
Active material	Control	CF1	CF2	CF3
current density (mA/cm^2)	-3.2	-5.5	-7.7	-4.6
Current density of CF2 @ different rpm				

rpm	100	400	900	1600	2500	3600
mA/cm^2	-2.6	-4.5	-6.2	-7.7	-8.7	-9.1

4. Conclusion

The synergy between a strong catalytic chemistry of metal oxide composite materials and the sustainable carbon material gives a path towards low cost, earth abundant, renewable, and well-being electrocatalysts. The successfully synthesised carbon-metal composite (C@Fe_3C/Fe_3O_4) via carbonization method shows uniform distribution Fe_3C/Fe_3O_4 nanoparticles on the partially graphitized layered carbon surface. Due to the synergetic effect between heterosystem, the C@Fe_3C/Fe_3O_4 also shows an impressive catalytic performance toward the ORR and catalytic stability up to 18 h. The 4e$^-$ reaction (less H_2O_2 formation) suggests that our electrocatalyst may have an impact on efficient electrocatalyst designing for ORR in alkaline solution.

Table 3: Comparative ORR performance for Iron based active material.

Active material	**Onset potential**	**Limiting current density**	**n (e$^-$)**	**Electrolyte**	**Reference**
	(V vs RHE)	(mA cm^{-2})			
Fe/FeN@N-C-2-800	0.87	6.04	~4	0.1 M KOH	[47]
$ZnCl_2$-Fe/C/N@bio-C	0.89	6.20	4	0.1 M KOH	[48]
Fe-Nx-C-2	0.92	6.50	~4	0.1 M KOH	[49]
Fe/S-NC	1.00	4.30	3.92	0.1 M KOH	[50]
mFe_3O_4@C NPs	-0.05	5.22	~4	0.1 M KOH	[51]
Fe-N-C/Fe_3C/C-S-C nanohybrid	1.08	5.80	4.03	0.1 M KOH	[52]
Fe_3N/Fe-N-C	0.85	5.99	~4	0.1 M KOH	[53]

Fe/N-C	0.81	5.43	3.98	50 mM PBS	[54]
$Fe_3O_4/Fe_3C@C$	0.86	-9.1	3.7-3.8	0.1 M KOH	**This work**

Acknowledgement

SRM expresses gratitude to Jain University for providing a Junior Research Fellowship. MS appreciates the financial support of the SERB in New Delhi, India, for supporting the research (EMR/2017/003368). The authors thank the FESEM and PXRD facilities provided by the NANOMISSION project (SR/NM/NS-20/2014). The authors gratefully appreciate the TEM Facility, which was supported by a TPF Nanomission, GoI project, and Raman characterization at the Centre for Nano and Soft Matter Sciences in Bengaluru, India, as well as XPS characterization at the Indian Institute of Technology Kanpur in Kanpur, India.

Reference

1. Z. Pu, G. Zhang, A. Hassanpour, D. Zheng, S. Wang, S. Liao, Z. Chen and S. Sun, *Applied Energy*, 2021, **283**, 116376.
2. A. Lim, H.-Y. Jeong, Y. Lim, J. Y. Kim, H. Y. Park, J. H. Jang, Y.-E. Sung, J. M. Kim and H. S. Park, *Science Advances*, 2021, **7**, eabf7866.
3. Z. Khan, M. Vagin and X. Crispin, *Advanced Science*, 2020, **7**, 1902866.
4. Z. Khan, B. Senthilkumar, S. O. Park, S. Park, J. Yang, J. H. Lee, H.-K. Song, Y. Kim, S. K. Kwak and H. Ko, *Journal of Materials Chemistry A*, 2017, **5**, 2037-2044.
5. S. Wang, L. Zhang, Z. Xia, A. Roy, D. W. Chang, J.-B. Baek and L. Dai, *Angewandte Chemie International Edition*, 2012, **51**, 4209-4212.
6. W. Xiao, M. A. Liutheviciene Cordeiro, M. Gong, L. Han, J. Wang, C. Bian, J. Zhu, H. L. Xin and D. Wang, *Journal of Materials Chemistry A*, 2017, **5**, 9867-9872.
7. R. J. Farrauto, M. Deeba and S. Alerasool, *Nature Catalysis*, 2019, **2**, 603-613.
8. V. Beermann, M. Gocyla, S. Kühl, E. Padgett, H. Schmies, M. Goerlin, N. Erini, M. Shviro, M. Heggen, R. E. Dunin-Borkowski, D. A. Muller and P. Strasser, *Journal of the American Chemical Society*, 2017, **139**, 16536-16547.
9. C. Zhang, J. Sha, H. Fei, M. Liu, S. Yazdi, J. Zhang, Q. Zhong, X. Zou, N. Zhao, H. Yu, Z. Jiang, E. Ringe, B. I. Yakobson, J. Dong, D. Chen and J. M. Tour, *ACS Nano*, 2017, **11**, 6930-6941.
10. X. Yue, C. He, C. Zhong, Y. Chen, S. P. Jiang and P. K. Shen, *Advanced Materials*, 2016, **28**, 2163-2169.
11. S. Zhen, W. Sun, P. Li, G. Tang, D. Rooney, K. Sun and X. Ma, *Journal of Power Sources*, 2016, **315**, 140-144.
12. J. Masud and M. Nath, *ACS Energy Letters*, 2016, **1**, 27-31.
13. S. Rojas-Carbonell, C. Santoro, A. Serov and P. Atanassov, *Electrochemistry Communications*, 2017, **75**, 38-42.

14. Z.-Y. Zu, J.-L. Mi, B. Wu and L. Liu, *ChemCatChem*, 2020, **12**, 5780-5788.
15. K. Mao, L. Yang, X. Wang, Q. Wu and Z. Hu, *The Journal of Physical Chemistry Letters*, 2020, **11**, 2896-2901.
16. M. Wu, M. Cui, L. Wu, S. Hwang, C. Yang, Q. Xia, G. Zhong, H. Qiao, W. Gan, X. Wang, D. Kline, M. R. Zachariah, D. Su, T. Li and L. Hu, *Advanced Energy Materials*, 2020, **10**, 2001119.
17. Y. Mu, Z. Ai and L. Zhang, *Environmental Science & Technology*, 2017, **51**, 8101-8109.
18. Z. Liu, Z. Zhao, Y. Wang, S. Dou, D. Yan, D. Liu, Z. Xia and S. Wang, *Advanced Materials*, 2017, **29**, 1606207.
19. P. Zhang, J.-S. Wei, X.-B. Chen and H.-M. Xiong, *Journal of Colloid and Interface Science*, 2019, **537**, 716-724.
20. M. Wang, Y. Li, J. Fang, C. J. Villa, Y. Xu, S. Hao, J. Li, Y. Liu, C. Wolverton, X. Chen, V. P. Dravid and Y. Lai, *Advanced Energy Materials*, 2020, **10**, 1902736.
21. L. Lai, J. R. Potts, D. Zhan, L. Wang, C. K. Poh, C. Tang, H. Gong, Z. Shen, J. Lin and R. S. Ruoff, *Energy & Environmental Science*, 2012, **5**, 7936-7942.
22. J.-C. Li, P.-X. Hou and C. Liu, *Small*, 2017, **13**, 1702002.
23. W.-J. Niu, Y.-P. Wang, J.-Z. He, W.-W. Liu, M.-C. Liu, D. Shan, L. Lee and Y.-L. Chueh, *Nano Energy*, 2019, **63**, 103788.
24. L. Chai, L. Zhang, X. Wang, L. Xu, C. Han, T.-T. Li, Y. Hu, J. Qian and S. Huang, *Carbon*, 2019, **146**, 248-256.
25. X. Chen, N. Wang, K. Shen, Y. Xie, Y. Tan and Y. Li, *ACS Applied Materials & Interfaces*, 2019, **11**, 25976-25985.
26. D. Ding, K. Shen, X. Chen, H. Chen, J. Chen, T. Fan, R. Wu and Y. Li, *ACS Catalysis*, 2018, **8**, 7879-7888.
27. Y. Jing, Y. Cheng, L. Wang, Y. Liu, B. Yu and C. Yang, *Chemical Engineering Journal*, 2020, **397**, 125539.
28. F. L. Meng, Z. L. Wang, H. X. Zhong, J. Wang, J. M. Yan and X. B. Zhang, *Advanced materials (Deerfield Beach, Fla.)*, 2016, **28**, 7948-7955.
29. W. Gu, L. Hu, J. Li and E. Wang, *Electroanalysis*, 2018, **30**, 1217-1228.
30. C. Wang, F. Yang, T. Qiu, Y. Cao, H. Zhong, C. Yu, R. Li, L. Mao and Y. Li, *Journal of Electroanalytical Chemistry*, 2018, **810**, 62-68.
31. C. Cao, L. Wei, Q. Zhai, J. Ci, W. Li, G. Wang and J. Shen, *ACS Applied Materials & Interfaces*, 2017, **9**, 22465-22475.
32. Q. Wang, Z.-Y. Zhou, Y.-J. Lai, Y. You, J.-G. Liu, X.-L. Wu, E. Terefe, C. Chen, L. Song, M. Rauf, N. Tian and S.-G. Sun, *Journal of the American Chemical Society*, 2014, **136**, 10882-10885.
33. Z. Zhang, S. Yang, H. Li, Y. Zan, X. Li, Y. Zhu, M. Dou and F. Wang, *Advanced Materials*, 2019, **31**, 1805718.
34. K. Kaare, E. Yu, A. Volperts, G. Dobele, A. Zhurinsh, A. Dyck, G. Niaura, L. Tamasauskaite-Tamasiunaite, E. Norkus, M. Andrulevičius, M. Danilson and I. Kruusenberg, *ACS Omega*, 2020, **5**, 23578-23587.
35. X. Tian, X. F. Lu, B. Y. Xia and X. W. Lou, *Joule*, 2020, **4**, 45-68.
36. S. Pérez-Rodríguez, D. Sebastián, C. Alegre, T. Tsoncheva, N. Petrov, D. Paneva and M. J. Lázaro, *Electrochimica Acta*, 2021, **387**, 138490.
37. S. R. Manippady, A. Singh, C. S. Rout, A. K. Samal and M. Saxena, *ChemElectroChem*, 2020, **7**, 1928-1934.
38. S. Haghdan, S. Renneckar and G. D. Smith, in *Lignin in Polymer Composites*, eds. O. Faruk and M. Sain, William Andrew Publishing, 2016, DOI: https://doi.org/10.1016/B978-0-323-35565-0.00001-1, pp. 1-11.
39. Z. Q. Li, C. J. Lu, Z. P. Xia, Y. Zhou and Z. Luo, *Carbon*, 2007, **45**, 1686-1695.
40. D. D. Hawn and B. M. DeKoven, *Surface and Interface Analysis*, 1987, **10**, 63-74.
41. I. N. Shabanova and V. A. Trapeznikov, *Journal of Electron Spectroscopy and Related Phenomena*, 1975, **6**, 297-307.

42. G. Zhong, S. Xu, L. Liu, C. Z. Zheng, J. Dou, F. Wang, X. Fu, W. Liao and H. Wang, *ChemElectroChem*, 2020, **7**, 1107-1114.
43. M. Shao, Q. Chang, J.-P. Dodelet and R. Chenitz, *Chemical Reviews*, 2016, **116**, 3594-3657.
44. M. Rana, S. Mondal, L. Sahoo, K. Chatterjee, P. E. Karthik and U. K. Gautam, *ACS Applied Materials & Interfaces*, 2018, **10**, 33737-33767.
45. Z. Khan, S. O. Park, J. Yang, S. Park, R. Shanker, H.-K. Song, Y. Kim, S. K. Kwak and H. Ko, *Journal of Materials Chemistry A*, 2018, **6**, 24459-24467.
46. H. Meng, Y. Liu, H. Liu, S. Pei, X. Yuan, H. Li and Y. Zhang, *ACS Applied Materials & Interfaces*, 2020, **12**, 41580-41589.
47. C. Feng, Y. Guo, S. Qiao, Y. Xie, L. Zhang, L. Zhang, W. Wang and J. Wang, *Applied Surface Science*, 2020, **533**, 147481.
48. Y. Li, H. Hu, J. Song, Y. Wu, X. Lv, Z. Xiao, F. Wang and Y. Chen, *Energy Technology*, 2020, **8**, 2000625.
49. L. Gao, M. Xiao, Z. Jin, C. Liu, J. Ge and W. Xing, *Journal of Energy Chemistry*, 2019, **35**, 17-23.
50. P. Zhang, C. Chen, X. Zhang, Z. Jiang, J. Huang and J. Chen, *Electrochimica Acta*, 2019, **298**, 570-579.
51. J. Zhao, C. Li and R. Liu, *Nanoscale*, 2018, **10**, 5882-5887.
52. A. Al-Shahat Eissa, N. H. Kim and J. H. Lee, *Journal of Materials Chemistry A*, 2020, **8**, 23436-23454.
53. N. Xue, J. Liu, P. Wang, C. Wang, S. Li, H. Zhu and J. Yin, *Journal of Colloid and Interface Science*, 2020, **580**, 460-469.
54. Z. Fan, J. Li, W. Yang, Q. Fu, K. Sun, Y.-C. Song, Z. Wei, Q. Liao and X. Zhu, *Chemical Engineering Journal*, 2020, **385**, 123393.